Miniaturized electromechanical devices for the characterization of the biomechanics of deep tissue

Enming Song [1,2,18], Zhaoqian Xie [3,4,18], Wubin Bai [5,6,18], Haiwen Luan [5,18], Bowen Ji[7], Xin Ning[8], Yu Xia[9], Janice Mihyun Baek[9], Yujin Lee[9], Raudel Avila[10], Huang-Yu Chen[5], Jae-Hwan Kim[9], Surabhi Madhvapathy[5], Kuanming Yao[2], Dengfeng Li[2], Jingkun Zhou[2], Mengdi Han[5], Sang Min Won[11], Xinyuan Zhang[12], Daniel J. Myers[5,13], Yongfeng Mei[12], Xu Guo[3,4], Shuai Xu[5,13], Jan-Kai Chang [5 ✉], Xinge Yu [2 ✉], Yonggang Huang [5,10,14,15 ✉] and John A. Rogers [5,10,15,16,17 ✉]

Evaluating the biomechanics of soft tissues at depths well below their surface, and at high precision and in real time, would open up diagnostic opportunities. Here, we report the development and application of miniaturized electromagnetic devices, each integrating a vibratory actuator and a soft strain-sensing sheet, for dynamically measuring the Young's modulus of skin and of other soft tissues at depths of approximately 1–8 mm, depending on the particular design of the sensor. We experimentally and computationally established the operational principles of the devices and evaluated their performance with a range of synthetic and biological materials and with human skin in healthy volunteers. Arrays of devices can be used to spatially map elastic moduli and to profile the modulus depth-wise. As an example of practical medical utility, we show that the devices can be used to accurately locate lesions associated with psoriasis. Compact electronic devices for the rapid and precise mechanical characterization of living tissues could be used to monitor and diagnose a range of health disorders.

Technologies for rapid, in vivo assessments of soft-tissue biomechanics have potential for broad utility in biological research and clinical diagnostics[1,2]. Of particular interest are advanced electromechanical systems that enable precise measurements of mechanical properties of tissues[3] to provide diagnostic utility, to track responses to treatment and to evaluate small but clinically meaningful deterioration for a range of dermatological conditions. For example, characterization of soft-tissue biomechanics may guide objective assessments of disease severity for oedema associated with lower venous leg disorders[4] or scleroderma, a lethal rheumatological and dermatological disease that currently depends on subjective physician grading scales[5]. An important focus is on the elastic modulus (the relationship between strain and stress) as the basis for evaluations of these diseases[1]. Additional possibilities include tracking of wound-healing cascades and tissue growth, regeneration and ageing, each of which involves changes in the elastic modulus of the surface and/or subsurface layers[6–9]. Conventional methods for characterization rely on quasi-static measurements of displacement as a function of applied forces delivered via suction,

torsion, compression or indentation[10–15]. An alternative known as magnetic resonance elastography yields quantitative measurements of the elastic modulus, including spatial–temporal maps of tissue stiffness[16,17]. Although useful in many scenarios, these techniques involve elaborate set-ups and require trained practitioners, which are barriers for their simple, rapid use outside hospital and laboratory settings and for application as direct diagnostic evaluations during surgical procedures. Also, in many cases, the necessary tissue interfaces can lead to measurement uncertainties and difficulties in mounting on curved or textured surfaces.

Owing to their miniature dimensions and skin-compatible formats, emerging classes of biointegrated electronic systems may offer powerful alternatives[18,19]. Recent research establishes the use of thin, flexible piezoelectric actuators and/or sensors for the characterization of soft-tissue biomechanics, with measurements that rely on minute deformations of tissues at near-surface regions. Examples range from conformal sheets for high-resolution mapping of the elastic modulus near the surfaces of skin lesions[20] to needle-shaped penetrating probes for in vivo mechanical sensing for guidance in

[1]Institute of Optoelectronics, Fudan University, Shanghai, China. [2]Department of Biomedical Engineering, City University of Hong Kong, Hong Kong, China. [3]State Key Laboratory of Structural Analysis for Industrial Equipment, Department of Engineering Mechanics, Dalian University of Technology, Dalian, China. [4]Ningbo Institute of Dalian University of Technology, Ningbo, China. [5]Querrey Simpson Institute for Bioelectronics, Northwestern University, Evanston, IL, USA. [6]Department of Applied Physical Sciences, University of North Carolina at Chapel Hill, Chapel Hill, NC, USA. [7]Unmanned System Research Institute, Northwestern Polytechnical University, Xi'an, China. [8]Department of Aerospace Engineering, The Pennsylvania State University, University Park, PA, USA. [9]Frederick Seitz Materials Research Laboratory, University of Illinois at Urbana-Champaign, Urbana, IL, USA. [10]Department of Mechanical Engineering, Northwestern University, Evanston, IL, USA. [11]Department of Electrical and Computer Engineering, Sungkyunkwan University, Suwon, Republic of Korea. [12]Department of Materials Science, State Key Laboratory of ASIC and Systems, Fudan University, Shanghai, China. [13]Department of Dermatology, Feinberg School of Medicine, Northwestern University, Chicago, IL, USA. [14]Department of Civil and Environmental Engineering, Northwestern University, Evanston, IL, USA. [15]Department of Materials Science and Engineering, Northwestern University, Evanston, IL, USA. [16]Department of Biomedical Engineering, Northwestern University, Evanston, IL, USA. [17]Department of Neurological Surgery, Northwestern University, Evanston, IL, USA. [18]These authors contributed equally: Enming Song, Zhaoqian Xie, Wubin Bai, Haiwen Luan. ✉e-mail: jan-kai.chang@northwestern.edu; xingeyu@cityu.edu.hk; y-huang@northwestern.edu; jrogers@northwestern.edu

biopsies[21], to thin, flexible piezoresistive cantilevers as indentation sensors for characterization of cancerous breast tissues[3]. These and other related approaches differ from past technologies in their thin, flexible geometries and their ability to form minimally invasive interfaces on complex topographies and textures of biological surfaces[22,23]. An important mode of use is in locating and identifying aberrant tissues through abnormal elastic moduli that result from specific disease states[3,20,21,24]. In many cases, however, these methods focus on sensing only to superficial depths below the surface (that is, tens of micrometres or less, typically confined to the stratum corneum or upper layers of the epidermis for the case of skin)[20].

This paper presents a simple, miniature electromechanical system that can interface with biological tissues for precise, rapid evaluations (~1 min for an individual measurement) of their elastic modulus, at a range of frequencies and depths and across a variety of spatial scales, including two-dimensional mapping. These devices integrate components for mechanical actuation and sensing in a single package, using certain ideas adapted from those used as the basis of skin-integrated haptic interfaces for virtual/augmented reality[25]. The resulting capabilities can complement those of recently reported approaches for sensing biomechanics at superficial depths. The following sections describe the engineering concepts, with a focus on measurements of elastic moduli of biological targets averaged over depths that are tunable across the millimetre range (from 1 to 8 mm). Experimental and simulation studies demonstrate quantitative measurements of tissue moduli for a wide scope of coupling substrates and conditions, including bilayer test structures as illustrations of depth profiling. Examples range from mechanical evaluations of biomaterials (hydrogels) with moduli comparable to those of soft human tissues, to samples of skin from animal models, to various locations on human volunteers. The results define some envisioned applications, including those relevant to clinical evaluations of patients with skin disorders. Advanced versions incorporate arrays of such devices for large-area mapping of elastic moduli. These findings have broad potential for use in exploratory research, clinical medicine and at-home diagnostics.

Results and discussion

Materials, designs, integration schemes and performance characteristics. Figure 1a presents a schematic illustration and an image of a representative device, which we refer to as an electromechanical modulus (EMM) sensor. The stack comprises the following components: (1) a top layer that generates a time-dependent Lorenz force as the source for vibratory actuation (Fig. 1b); (2) a thin strain gauge in the form of a serpentine metal trace as the basis for mechanical sensing (Fig. 1c); and (3) a supporting thin elastomeric layer as a reversible, soft interface to a tissue surface. The total thickness of this example is ~2.5 mm and the contacting area is ~2 cm² (lower inset of Fig. 1a). The fabrication begins with the patterning of serpentine-shaped electrical traces as resistive strain gauges, followed by transfer printing onto a soft, flexible substrate (poly(dimethylsiloxane) (PDMS), ~30 μm thick). Thin gold (Au) lines form an open mesh structure (100-nm thick) to define a sensing area of ~0.5 cm² that is embedded above and below by layers of polyimide (1-μm thick), as illustrated in Fig. 1c,d. A sequence of assembly steps prepares the actuator and wired connections for integration with the underlying gauge to yield a functional system. The actuator includes a nickel-coated neodymium magnet (8 mm in diameter, 1.5-mm thick) mounted on a thin polyimide disc (75-μm thick) via a dual-sided adhesive and a copper coil on top (Cu, 50-μm wire diameter, 240 turns with an outer diameter of 12 mm, electrical resistance of ~70 Ω), as displayed in Fig. 1b. Here, the polyimide interlayer provides stable mechanics[26] that enables the efficient delivery of force from the magnet towards the underlying gauge. Detailed information is provided in Supplementary Figs. 1 and 2.

As illustrated in the equivalent circuit diagram in the upper inset of Fig. 1a, the magnet undergoes vibratory motions following the application of an alternating current through the copper coil (V_A; < 5 V, sine wave, 50 Hz), with a travelling amplitude of several hundreds of micrometres (Supplementary Video 1). The ring-shaped shell (PDMS, 2.4-mm thick) around the actuator defines sufficient space for out-of-plane motions of the magnet. The gap of ~1 mm between the coil and the magnet (1.5-mm thick) greatly exceeds the amplitude of motion of the magnet to avoid direct contact with the top coil during operation. Therefore, the vibratory motions of the magnets deliver pressures onto the bottom surface of the sensor due to inertial effects and directed deformations that extend to millimetre-scale depths of tissue. The result yields strains distributed over the metal traces of the strain gauge, which leads to periodic variations in electrical resistance. Analyses of these responses by performing simultaneous measurements of the voltage across the strain gauge (output voltage, V_S) via lock-in techniques allows quantitative determination of the elastic modulus of the tissues. Specifically, a constant current (I_S) delivered from a current source to the strain gauge (Supplementary Fig. 3) provides an input channel to the lock-in amplifier to capture the amplitudes of periodic variations in the gauge resistance as V_S at the frequency of the vibration. Supplementary Fig. 4a shows the measurement set-up for mechanical sensing on a sample of artificial skin. Existing methods for sensing tissue biomechanics at superficial depths (micrometre-scale) via the use of piezoelectric actuators/sensors[20,21] serve as a basis for comparison. The devices reported here mechanically couple with contacting tissues through millimetre-scale thicknesses, thereby enabling the characterization of deep tissue biomechanics at lengths defined by the geometry of the sensor, as described below. Information on the measurement mechanism and operational principles is provided in Supplementary Fig. 4b.

The sensors are mounted on tissues of interest via a thin layer of a soft elastomer (PDMS, 30-μm thick; an example, a forearm, is shown in Fig. 1e). Conformal contact occurs via lamination in a simple, reversible manner that enables multiple cycles of use (100 times). Figure 1f shows a device conformally mounted on the curved surface of the skin of the fingertip of a volunteer. The adhesive strength of the PDMS tape depends on the ratio of the base to crosslinker in the formulation and the number of cycles of application and removal from the skin[27]. Experiments show that, for sufficient adhesion, the adhesive strength does not affect the measurement result (Supplementary Fig. 5). As shown in Supplementary Fig. 6a, the overall electrical resistance of the strain gauge remains largely unchanged, to within experimental uncertainties, after 10³ cycles of bending into cylindrical shapes. The change in resistance as a function of bending radius (to values down to 3 cm) is shown in Supplementary Fig. 6b. The observed changes (~0.25%, 2–3 Ω) are small compared with the resistance of the strain gauge itself (~1 kΩ) and are reversible, consistent with the theoretical expectation[28]. The encapsulation layers (polyimide/PDMS, 1-μm/30-μm thick) isolate the system from moisture and biofluids. Specifically, the devices offer consistent performance before and after 7 days of immersion in artificial sweat solution at 50 °C (Supplementary Fig. 6c). With the actuator mounted on top, the devices offer stable measurement results on curved surfaces across a range of bending radii (>4 cm; Fig. 1g and Supplementary Fig. 7).

These simple designs and fabrication strategies yield reliable devices at high yields. Statistical data for the resistance of the strain gauge (R_{gauge}), the device yield and the signal-to-noise ratio (SNR) associated with 100 devices are presented in Supplementary Fig. 8. The yield corresponds to the percentage of functional devices, and the SNR is the ratio between V_S and the noise level with a sine wave with amplitude, V_A, of 5 V at a frequency, f, of 50 Hz in the top actuator, during measurements. Failure most typically follows from fractures in the strain gauge or from disconnections between the wires
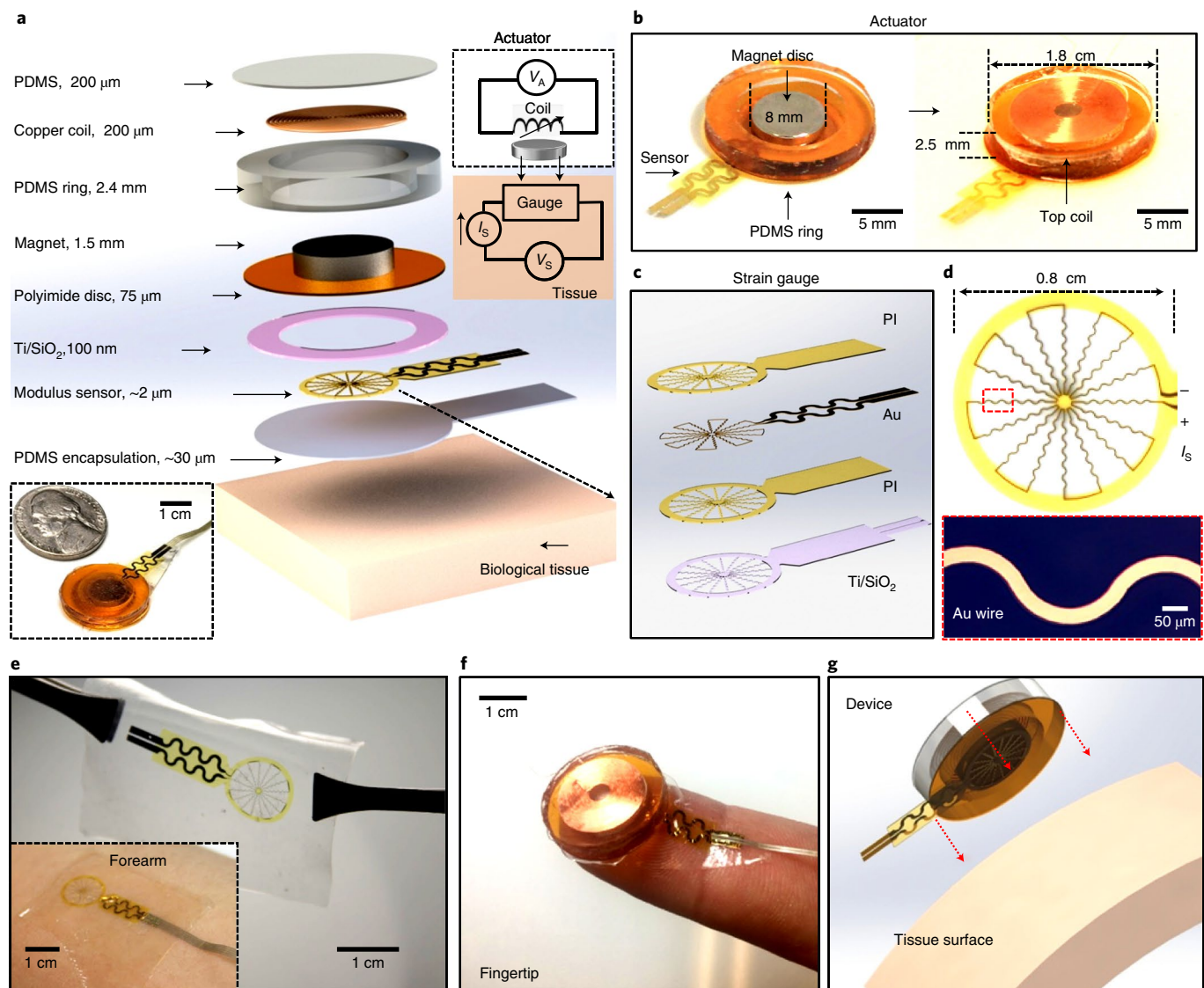
Fig. 1 | Millimetre-scale electromechanical systems for sensing of soft-tissue elastic moduli. a, Exploded-view schematic illustration of the system. Upper-right inset shows a circuit diagram with an input voltage for the actuator (V_A) and a sensing voltage from the gauge (V_S). Lower-left inset is a photograph of the back side of the system next to a US nickel coin. **b,** Photographs of the key constituent components of the system, including a disc magnet (left) and a copper coil (right). **c,** Magnified view of the layer configuration of the strain gauge. PI, polyimide. **d,** Schematic diagram of the strain gauge. **e,** Photograph of the strain sensor. Inset is an image of the gauge laminated onto the skin of the forearm. **f,** Photograph of the device on a fingertip. **g,** Scheme for coupling the system onto the surface of human skin.

of the coil in the actuator. These results suggest high levels of uniformity and consistency in device performance (for example, R_{gauge} of ~10^3 Ω, total yield of 96% and SNR of ~40 dB). Although this system can be applied to a range of biological tissues, the results reported here focus on human skin— from studies of healthy volunteers (Fig. 1g) and patients associated with a dermatology clinic—on various body locations, including curved surfaces of the face, forearm and shoulder (Supplementary Fig. 9).

Experimental and computational analyses of the device operation. For a given V_A and f, the magnet responds at the same frequency with an amplitude that depends on the properties of the sample and the parameters of the device (Methods). Placing the magnet directly above the strain gauge in the device structure maximizes the amplitude of the measured response and therefore the sensitivity (Fig. 2a). Using lock-in techniques, periodic variations in the resistances of these traces yield detectable changes in the signal

with high sensitivity following the application of a constant current I_S (1 mA). The magnitude of the strain, and therefore V_S, depends on the elastic modulus and thickness of the tissue. Finite element analysis (FEA) quantifies the mechanical coupling between the actuator, the sensor and the tissues. An example distribution of equivalent strain across the gauge structure is shown in Fig. 2a for measurements (V_A of 5 V at 50 Hz) on artificial skin substrates (PDMS, 1-cm thick) with elastic moduli of 10, 100 and 600 kPa. This range is relevant to human skin and other related tissues. The normalized strain in the gauge structure increases by a factor of approximately two as the tissue modulus decreases from 600 to 10 kPa, with a corresponding increase in V_S. Details of the FEA simulation is provided in the Supplementary Information.

The results shown in Fig. 2b and Supplementary Fig. 10 summarize the dependence of the amplitude of the motion of the magnet on V_A and f during operation on a sample of artificial skin (PDMS, 3-mm thick, 200 kPa). Here, different weight ratios of crosslinker in
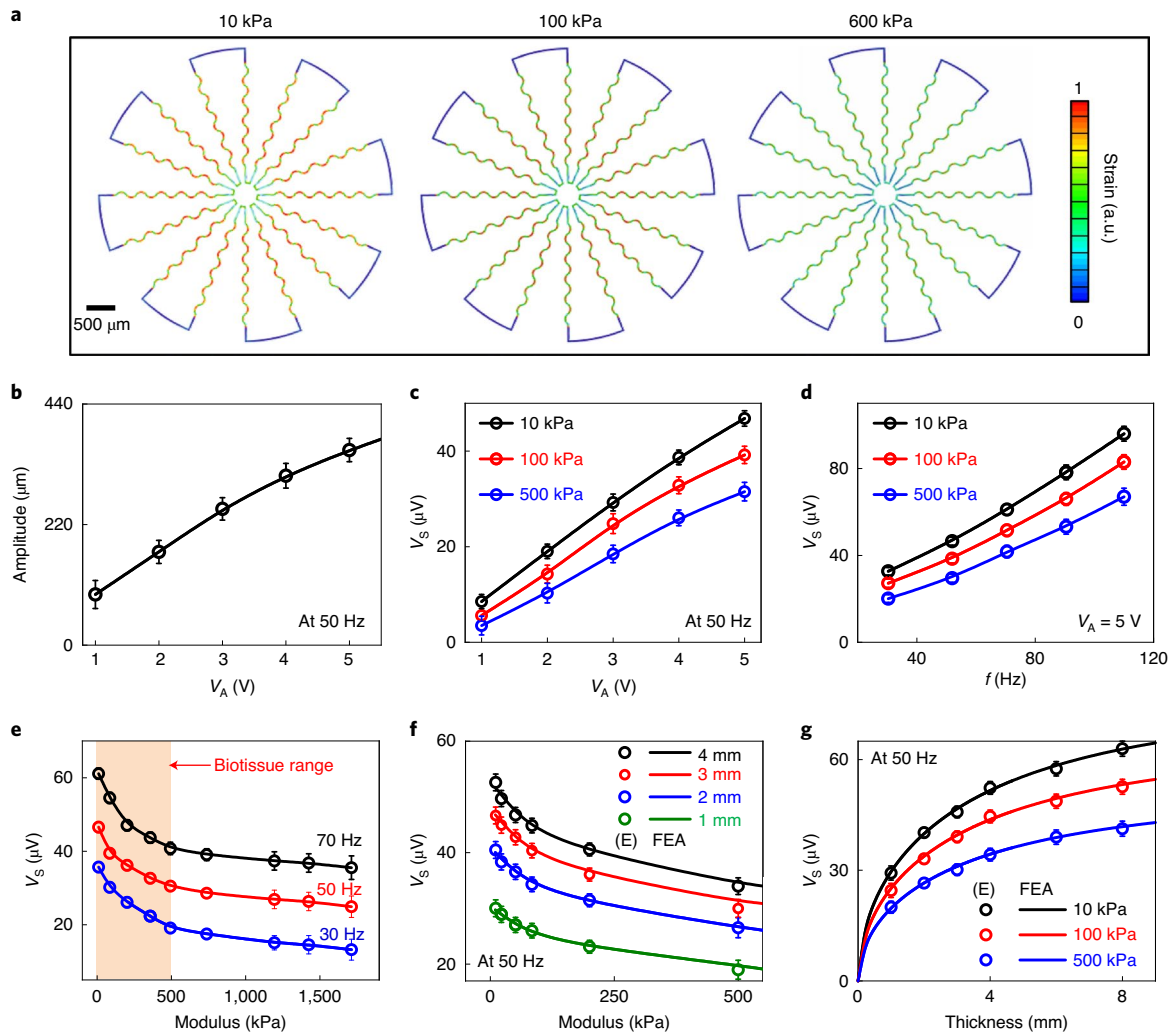
Fig. 2 | Experimental and simulation results of the device operation. a, FEA simulation results (in arbitrary units (a.u.)) for the distribution of maximum strain across the gauge on artificial skin samples with elastic moduli of 10, 100 and 600 kPa. **b**, Vibrational amplitude of the magnet as a function of the amplitude of sine-wave input voltage (V_A) while in contact with an artificial skin sample with a modulus of 200 kPa. **c,d**, V_S as function of V_A (**c**) and actuation frequency (**d**). **e**, V_S as a function of the modulus at various frequencies. **f**, Experimental (E, circles) and simulation (FEA, line) results for V_S as a function of the sample modulus with various sample thicknesses. **g**, V_S as a function of the thicknesses of samples with various moduli. The circles and lines correspond to experimental (E) and simulation (FEA) results, respectively. For all cases, centre values are shown, and error bars correspond to the standard deviation for at least ten measurements with a given device.

the PDMS samples yield various desired moduli for these substrates. Independent measurements of the elastic modulus exploit a biosoft intender under quasi-static conditions (Supplementary Fig. 11). A high-speed camera allows direct visualization of the motions of the magnet during operation (Supplementary Video 2) as a means of measuring amplitudes as small as hundreds of micrometres (see Methods for details). The amplitude increases with V_A, with values of ~300 μm at a V_A of 5 V at 50 Hz (Fig. 2b), and depends on f, with a resonance at ~200 Hz (Supplementary Fig. 10), which is consistent with results reported in recent publications[25]. This resonance frequency is associated with the device structure and the mechanical properties of the contacting skin, whereby the polyimide disc and skin provide restoring force for the periodic vibration of the magnet.

The force generated by the magnet can be quantified. Supplementary Fig. 12a presents the strain measurements during magnet vibration on different thicknesses of artificial skin (PDMS, 200 kPa). Here, a thin, flexible piezoresistive force sensor, placed between the actuator and artificial skin, serves as a force sensor and

enables the recording of the periodic force generated by the magnet for each condition[29]. The results presented in Supplementary Fig. 12b show that the generated force and associated strain increase with the thickness of the tissue. This trend corresponds to an increase in the deformation at the measurement interface and a corresponding increase in the strain consistent with the results shown in Fig. 2g. The force applied to the skin can be increased by applying an additional positive direct current bias to V_A and by changing the sine-wave V_A to a square-wave voltage with the same amplitude. The former directs force to the magnet and the latter increases the effective input power to the top coil (Supplementary Fig. 13).

As the alternating current drives the actuators, the force delivered by the magnet yields a time-domain signal from the EMM sensor at the same frequency with an amplitude that depends on the mechanics of the tissue. The lock-in technique determines the amplitude of the periodic signal, V_S. Specifically, this signal can be recorded by a bioamplifier (Supplementary Fig. 14) during actuation, with a settling time as small as ~0.3 s (details provided in the

Supplementary Information). The amplitude of the signal (that is, V_S) increases with increasing tissue thickness and decreasing tissue modulus (Supplementary Fig. 15), as described below. According to previous reports[21], the viscoelastic effects of typical biological samples are negligible at the relatively low operating frequencies explored here (<1,000 Hz), such that measurements can be considered quasi-static. As such, V_S relates to the static modulus of elasticity, as per the FEA results. Figure 2c,d presents V_S values for artificial skin samples with elastic moduli of 10, 100 and 500 kPa (3-mm thick) as a function of V_A and f. The value of V_S increases with V_A (from 1 to 5 V) and f (from 30 to 110 Hz), consistent with the trends in the amplitudes of the motions of the magnet (Fig. 2b and Supplementary Fig. 10). Here, samples with a high modulus lead to a low strain and therefore a low V_S, which is in agreement with the FEA results (Fig. 2a). An important engineering consideration is that the coil can create electromagnetic induction effects on the gauge during measurements, thus generating some cross-talk with V_S at high frequencies (~10 μV at 1,000 Hz with V_A of 5 V; see Supplementary Fig. 16 for details). Decreasing the distance between the coil and the strain gauge further enhances the induced voltage to levels comparable to those of the sensor signals, adversely affecting operation of the device (Supplementary Fig. 17). Consequently, this consideration favours low-frequency operation (<100 Hz; red in Supplementary Fig. 16) and a sufficient gap between the coil and the strain gauge, where such inductive effects induce voltages that are approximately two orders of magnitude lower than those associated with the sensor signals. Unless otherwise stated, the subsequent studies use a fixed f (for example, 50 Hz) and V_A (5 V).

Figure 2e demonstrates that the value of V_S decreases with increasing modulus (10 kPa to 2 MPa) at various f values (30, 50 and 70 Hz) for samples of artificial skin with thicknesses of 3 mm, each supported by a glass wafer (Supplementary Fig. 11) to simulate underlying bones. In the low-modulus regime, the actuator vibrates relatively freely, with correspondingly high levels of localized deformation, large strains and therefore large V_S. For a high modulus, the sample limits the deformations, thereby yielding a small V_S. Samples with moduli less than 500 kPa (red in Fig. 2e) are of particular interest because they are most relevant to many soft biological tissues. Such samples yield a high sensitivity to the output V_S (Fig. 2f). The experimentally measured (circles) and FEA-simulated (lines) V_S in Fig. 2f vary consistently with moduli from 10 to 500 kPa. Here, increasing the thickness also increases the V_S, mostly due to decreasing effects of the rigid support (glass wafer) in limiting the deformations. These results show good detection sensitivity and measurement accuracy across elastic moduli (<500 kPa) relevant to those of most soft biological tissues in humans. For example, recent publications report skin modulus values in the small strain regime that fall within this range[1], such as the Young's modulus of the dermis and subcutaneous fat (~200 kPa and ~60 kPa)[30,31], which indicates the broad applicability of the EMM device designs reported here for measuring skin and tissue stiffness[1]. The stratum corneum and epidermis, which have comparatively large moduli[32], can be measured via methods based on recently described piezoelectric systems[20]. Figure 2g summarizes FEA and experimental results for the thickness dependence of V_S for different tissue moduli. The thickness effects diminish as the thickness of the target increases to values larger than several millimetres, which defines a saturation depth (7–8 mm) for the measurements, as demonstrated in Fig. 2g. Such characteristic depths can provide measurements across various tissue structures such as the surface layers of the skin (typically ~2-mm thick), subcutaneous fat and even underlying muscle[31]. As shown in Supplementary Fig. 18, the results reveal the dependence of V_S on the tissue modulus for samples with thicknesses (2 cm) that exceed the saturation depth.

An analytical expression can be determined for the output voltage $V_S = f(E, H$ and $V_A)$ in the case of small deformations (equation

(1)) by fitting the experimental and simulation data (Supplementary Fig. 19) as follows:

$$V_S = C(E) \tanh \left[\left(\frac{H}{H_0} \right)^{1/2} \right] V_A \qquad (1)$$

where the V_S is linearly proportional to the input V_A (5 V in the current experiments) in this regime of small deformations, H is the thickness of the target tissue and H_0 is the saturation depth. $C(E)$ is a dimensionless coefficient that depends on the elastic modulus (E) of the tissue (Supplementary Table 1 presents values obtained from FEA results). For a given device design, the measured V_S and H (determined by ultrasound) together with equation (1) and the values presented in Supplementary Table 1, provide a simple yet accurate way to determine the modulus of the target tissue. The dimensionless coefficient C should only depend on the non-dimensional, normalized tissue modulus, such as the ratio of E to the effective modulus of the device.

Measurements on hydrogels and on porcine and human skin. The EMM sensor can characterize the mechanical properties of a range of biomaterials and skin regions both ex vivo and in vivo (Fig. 3). Recent research shows that hydrogels (poly(ethyleneglycol) diacrylate) at different levels of hydration (water concentration) have Young's moduli that span those associated with most soft biological tissues in animal models and in humans[33,34]. Figure 3a presents results from samples with various levels of hydration and at a thicknesses of ~4 mm (inset of Fig. 3a). The V_S increases with increasing hydration from 30 wt% to 80 wt%. The results in Fig. 2g show corresponding values of the elastic modulus, as in Fig. 3b (blue), that range from ~37 kPa to ~1.5 MPa, which is consistent with the values (green in Fig. 3b) obtained using a biosoft indenter. This technique enables a quantitative analysis of the Young's modulus within the elastic regime via measurements of indentation force as a function of displacement (that is, strain)[35]. Similarly, Fig. 3c shows results obtained with samples of abdominal porcine skin (2-mm thick; inset of Fig. 3c). Here, increasing the hydration level to 40 wt% yields a V_S of ~34 μV. The comparisons are quantitatively consistent with measurements using the indenter for each hydration level, corresponding to a range from 95 kPa to ~1 MPa (Fig. 3d).

Dynamic mechanical analysis (DMA) represents another conventional technique for determining the Young's moduli of biological tissues through measurements of quasi-static, tensile stress–strain responses[36]. The results in Supplementary Fig. 20 summarize measurements of porcine skin via DMA at different hydration levels (from 10% to 40%). The results are in good agreement with those obtained using the EMM devices. Details on the preparation steps and measurement results are provided in the Methods. As a comparison, Supplementary Fig. 21 summarizes the measurement results on different types of ex vivo targets, including an artificial-skin model (PDMS), a sample of porcine skin (hydration level of 25%) and a sample of porcine muscle, with comparisons of measurements performed using EMM devices on standard samples to those obtained with conventional ex vivo testing methods. These three methods yield consistent results.

Capabilities extend to direct measurements of skin at various locations of the body of human volunteers, as illustrated in Fig. 3e. A collection of photographs illustrate applications across main regions of the body (for example, biceps, abdomen, thigh and forearm). The repeatability of measurements at a specific location represents an important metric. Results of multiple cycles of measurement from the forearm (Fig. 3f; that is, ten times) show that the average and standard deviation of V_S are 47.5 μV and 0.8 μV, respectively. The inset of Fig. 3f shows that the noise decreases with the square root of averaging time for an individual measurement (that is,
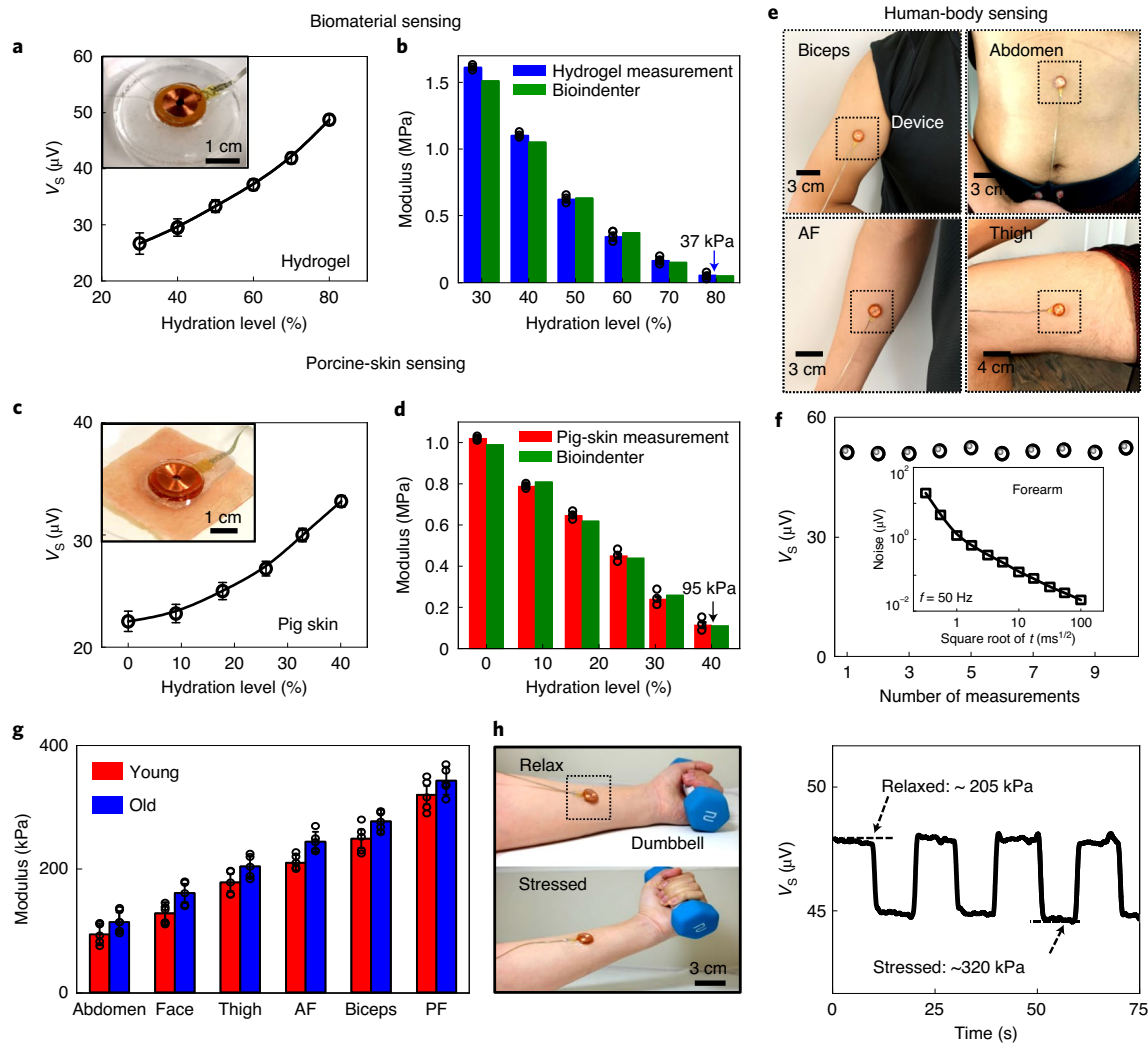
Fig. 3 | Modulus measurements on hydrogels and on porcine and human skin. a, V_S as a function of weight percentage of water of a hydrogel sample. Inset shows the device on an ~4-mm-thick sample of hydrogel during measurements. **b**, Moduli measured using an EMM sensor (blue) and values determined using a biosoft indenter (green), with various water contents of the hydrogel. **c**, V_S as a function of weight percentage of water in porcine skin. Inset shows the device on a sample of porcine skin (2-mm thick). **d**, Moduli measured using an EMM sensor (red) and indenter (green). In **a–d**, three individual measurements on different targets for a given device are shown, with error bars representing the standard deviation in each case. **e**, Photographs of devices on different locations of the human body. **f**, Repeatability of measurements as a function of the number of measurements at the same location on the forearm. Inset shows the noise for a representative measurement on the forearm as a function of the square root of the integration time (t) configured on the lock-in amplifier. **g**, Modulus measurements for different locations on the human body in young ($n=5$ aged 25–35 years) and old ($n=5$, aged 55–65 years) participants. Error bars correspond to the standard deviation for measurements among the participants, with corresponding centre values and dispersion measure shown. **h**, Dynamic measurements for modulus sensing. Left: photographs of the forearm before (upper) and after (lower) lifting a dumbbell. Right: V_S as a function of time during signal recording at a sampling frequency of 5 Hz. AF, anterior forearm; PF, posterior forearm.

integration time, t; the duration of a measurement operation that yields the value of V_S). As an example, increasing the integration time from 1 ms to 10 s decreases the noise from ~1 μV to ~10^{-2} μV, approximately two orders of magnitude smaller than the signal. As a result, the devices allow short measurement times (<1 min) and low noise levels.

Furthermore, the devices operate well on both hair-bearing and hairless areas of the skin (Supplementary Fig. 22) due to the ability of the bottom PDMS-encapsulated component to conform around isolated hair filaments. Curved surfaces of the skin have only a minor influence on measurements for radii of curvature larger than ~4 cm (for example, two times larger than the diameter of the device; Supplementary Fig. 7a,c). Failures in measurements can,

however, occur in extreme conditions (for example, the curvature associated with the nose bridge or hair associated with a beard) due to poor contact (Supplementary Fig. 7b).

The measurements depend on the tissue modulus (Fig. 2f) and, in certain cases, on the thickness of this tissue and the modulus of the underlying materials (Fig. 2g). For example, measurements at soft-tissue locations (that is, the abdomen) can be different from those at bony regions (that is, the finger joints)[37], as shown experimentally in Supplementary Fig. 23. These effects can be treated explicitly by accounting for the depth of penetration of the measurement and its dependence on features of the device design. As a comparison, each location shown in Fig. 3e includes the skin, superficial fat and underlying muscle tissues, with a total tissue

thickness that exceeds the characteristic depth of the device[38–40]. The measurements determine the average elastic modulus of the skin/tissue to a depth of ~8 mm, as previously demonstrated in Fig. 2g. Studies that do not consider this thickness effect involve elastic moduli measurements at different locations on the body from five healthy volunteers aged between 25 and 32 years and five participants aged between 60 and 68 years (Fig. 3g; determination of the modulus values rely on results in Supplementary Fig. 17). The results are within expected values for human skin and ex vivo biomaterials determined in the small strain regime using techniques based on suction[11,12], torsion[13] and indentation[10]. Consistent with expectation and recent reports[2], the moduli increase with age, typically due to a loss in hydration[41] (Fig. 3b,d). Detailed information for these clinical tests is provided in the Methods. The modulus can also depend on tension in the skin due to nonlinear mechanical responses associated with collagen and elastin fibres in the dermis[42]. Skin tension typically decreases with increasing age[2], thereby reducing the apparent modulus[43]. Additional studies (Supplementary Fig. 24) involved participants with a high body–mass index (BMI; typically 30–35 kg m^{-2}) and those with a low BMI (19–24 kg m^{-2}), with five participants in each group. The EMM signals are higher for the former than for the latter group, as might be expected due to higher levels of subcutaneous fat (thickness from a few millimetres to centimetres and modulus of ~50 kPa)[30,44].

Muscle activity can also affect the moduli measured across depths associated with the devices reported here. An example in Fig. 3h shows a device on the forearm in a relaxed state and in a tensed condition due to lifting a dumbbell. Repetitive cycles of movements during real-time recordings of V_S yield moduli values that vary continuously between minimum and maximum values of 205 kPa and 320 kPa, respectively (details of dynamic measurements are provided in the Methods). These values correspond to average moduli of the skin and underlying muscles to a characteristic depth of ~8 mm. Recent studies based on ultrasound elastography report muscle moduli that exhibit a similar trend with increasing intensity of activation (for example, the modulus of biceps muscles increases by ~100 kPa due to activation)[45]. Supplementary Fig. 25 summarizes results of measurements on the forearm and thigh for a volunteer while standing, sitting and lying down. The signals do not depend on posture and they yield elastic moduli that are consistent with those described in other papers[45,46]. Such capabilities may support various applications of the devices in kinesiology and rehabilitation.

Results obtained from patients with skin diseases in clinical settings are presented in Supplementary Figs. 26 and 27. These measurements reveal localized variations in skin moduli associated with lesions. An artificial-skin model (Supplementary Fig. 26a,b) for this case combines a low-modulus silicone substrate (8-mm thick, 5 cm in diameter) as healthy skin (~100 kPa) with a local high modulus silicone insert in the centre (1 cm diameter, ~500 kPa) as the lesion. Measurements of the modulus in the central region and nearby surrounding parts yield expected results (Supplementary Fig. 26c). Evaluations of five patients (aged 28–37 years) with psoriasis distributed across various body regions (arm, hand and lower back) are presented in Supplementary Fig. 27 (details are in the Methods). This condition leads to lesions comprising red patches of thick, scaly skin (over 1 cm in diameter) and pathological changes in skin properties, such as thickness, stiffness and hydration[47,48]. An adhesive medical dressing placed over the structure and onto adjacent skin prevented relative motion during evaluations. The measurements yield modulus values for the lesions and for nearby regions of unaffected skin (Supplementary Fig. 27b,d,f) for each location. As expected, the lesions exhibit higher moduli than those of nearby skin, due primarily to differences in skin elasticity and hydration[49]. These simple measurements, consistent with previously reported results[1], have potential clinical application in rapidly identifying and targeting of skin lesions, with quantitative metrics that have promise as

diagnostic biomarkers for a range of skin conditions. Supplementary Table 2 summarizes different types of skin/tissue disorders and corresponding lesion mechanics compared with healthy conditions, assessed using various measurement methods[20,21,50–52]. The pathologies range from systemic sclerosis to oedema and tissue diseases such as hepatocellular carcinoma, all of which involve variations in the elastic modulus of the lesion area compared with those of healthy skin/tissues. Overall, most of the diseases presented in Supplementary Table 2 involve lesion modulus values that span across the range measurable via the EMM sensors with high sensitivity (10–500 kPa; Fig. 2f).

Although EMM sensors provide powerful capabilities for a precise, rapid evaluation of tissue biomechanics, a potential limitation is that the system reported here involves benchtop lock-in detection electronics. Ongoing efforts focus on the development of a complete wearable system to allow continuous monitoring of skin/tissue properties during daily life activities. A device design concept to address these requirements is provided in Supplementary Fig. 28, based on adapted versions of wireless methods used for other purposes[25]. Briefly, a signal processing technique and a microcontroller can replace the lock-in detection electronics, and a wireless communication module can allow communication with a portable consumer electronic device (that is, a smart phone). The overall system design exploits a flexible printed circuit board (~1-mm thick) that can be configured into a wearable format. Additional details appear in the Supplementary Information.

Miniaturized designs for multilayer biological targets. In addition to measuring the elastic modulus to relatively large depths (over 8 mm), the lateral dimensions of the devices can be reduced, guided by computational modelling, to reduce these depths to values approaching those of the dermis (~1 mm). In this context, the size of the magnet enables the evaluation of tissue moduli across a tunable characteristic depth, with capabilities for depth profiling of deep and superficial tissue biomechanics. As an example, Fig. 4a summarizes devices that have sensing areas (surface area of the magnet) with diameters (D) from 8 mm to 1.5 mm, all with magnets that have the same thickness (1.5 mm). Figure 4b shows experimental (circles) and simulated (lines) FEA results for V_S from devices with different D (3 mm and 1.4 mm) on a single, thick layer of artificial skin (PDMS, 2-cm thick) as a function of the elastic modulus. Here, reducing D decreases the contact area between the device and skin, which in turn leads to decreases in V_S for a given f (50 Hz) and V_A (5 V). Figure 4c shows the cross-sectional strain distributions obtained by FEA in a sufficiently thick tissue with an elastic modulus of 200 kPa subjected to pressure on the surface from devices with different D. The distributions exhibit saturation depths (red lines in Fig. 4c) that decrease with D (that is, ~8.2 mm for D = 8 mm, ~3.3 mm for D = 3 mm and ~1.6 mm for D = 1.5 mm), which is consistent with the experimental results (Fig. 2g and Supplementary Fig. 29). These results suggest the basis for depth profiling of the modulus, which is of relevance for many types of biological tissues.

Furthermore, combining the measurement results of two devices with an appropriate D allows determination of the modulus of each layer for a bilayer structure. For skin, the stratum corneum, epidermis and upper dermis (typically 1–2-mm thick) serve as protective barriers against environmental hazards for subcutaneous tissues that consist of superficial fat and connective muscles over bones. These layers exhibit different moduli and thicknesses. Figure 4d presents a bilayer architecture of silicone materials that approximates the structure of skin/tissue, fabricated with different thicknesses (H_A = 1.8 mm; H_B » 1 cm) and different moduli (E_A = 200 kPa; E_B = 50 kPa). Measurements using devices with different D can determine the equivalent mechanical properties of this bilayer structure. Here, V_S is 30 μV and 20 μV for devices with D of 3 mm and 1.5 mm, respectively. These V_S values depend on both the sensing area (D)
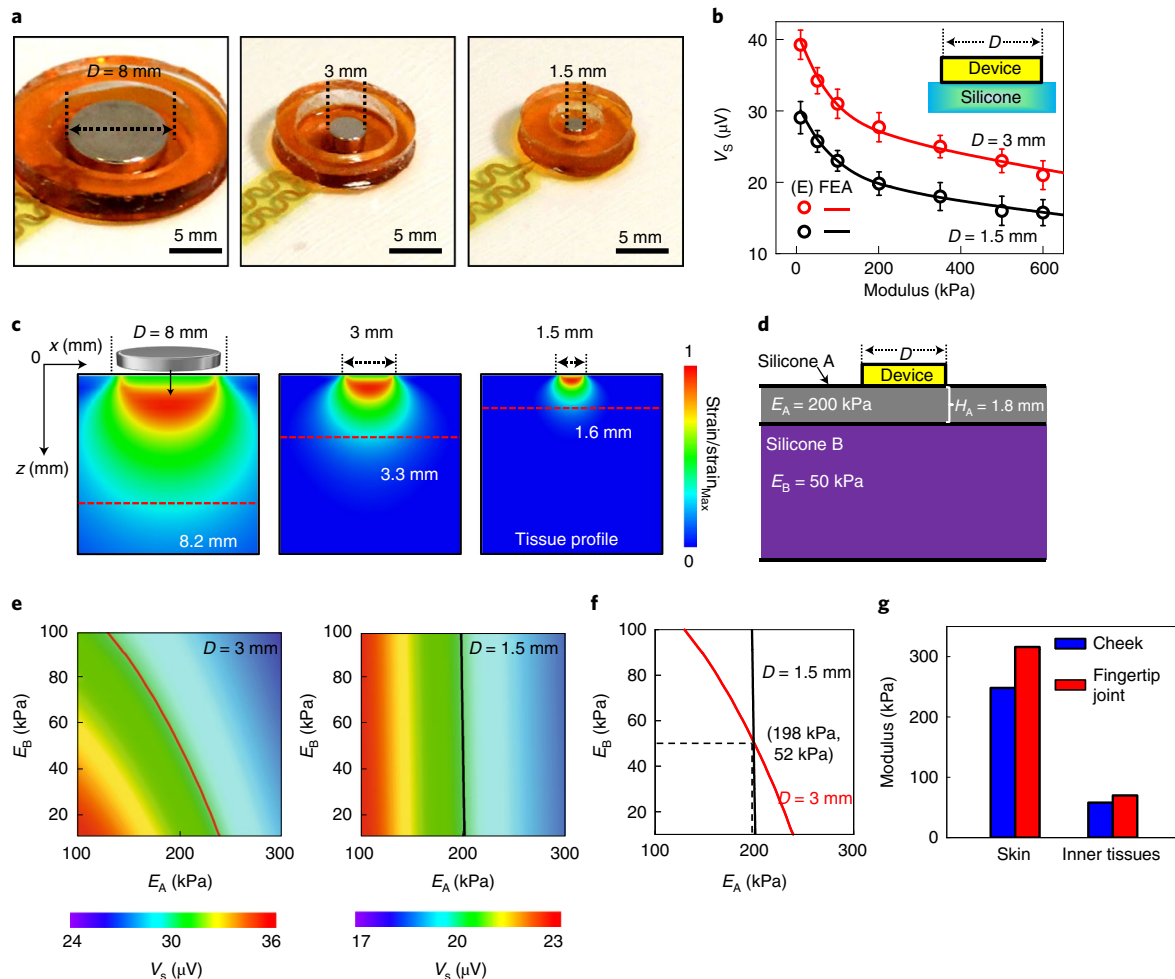
Fig. 4 | Designs for modulus sensing and depth profiling of multilayer samples. a, Photographs of devices with various sensing areas. **b**, Simulated (FEA, line) and measured (E, circles) V_S values for systems with different dimensions as a function of the elastic modulus for artificial skin samples. *D* represents the sensing diameter of the EMM sensor. Error bars correspond to the standard deviation for ten measurements with a given device with different *D*. **c**, Normalized FEA results for distributions of strain throughout the tissue structure with a modulus of 200 kPa, shown in the cross-sectional profile during actuator vibration, with different *D*. *z* is the depth into the tissue and *x* corresponds to the direction along the surface. The effective saturation depths decrease with decreasing *D* from 8 mm to 1.3 mm. **d**, Schematic illustration of a bilayer structure that approximates the skin/tissue system, with modulus values of 200 kPa and 50 kPa, and with thicknesses of 1.8 mm and >>1 cm, for the top and bottom layers, respectively. **e,f**, FEA modelling to determine the modulus of each layer in the bilayer structure from measurements using EMM sensors with different *D* (**e**), yielding simulation results for E_A and E_B (**f**). **g**, Simulated results of moduli for the skin and underlying tissues of the cheek and fingertip joint of a human participant.

and the modulus of each layer. Figure 4e shows the results of FEA simulation of V_S for layer moduli in the ranges of $E_A = 100–300$ kPa and $E_B = 10–100$ kPa, with different EMM sensors (*D* of 3 mm and 1.5 mm). For $V_S = 30$ μV and $D = 3$ mm, the simulated relationship between E_A and E_B, marked with the red curve, appears in the left of Fig. 4e. Similarly, for $V_S = 20$ μV and $D = 1.5$ mm, the relationship between E_A and E_B, marked with the black curve, appears in the right of Fig. 4e. The intersection of these two curves determines the calculated modulus for each layer as 198 kPa and 52 kPa for E_A and E_B (Fig. 4f), respectively, which are in excellent agreement (within 5% error) with the moduli of the sample in Fig. 4d. The above results depend on the thickness of each layer of tissue. For typical bilayer structures, a database for layers with different thicknesses can be used to determine the moduli of such bilayer structures.

To showcase this multilayer capability in clinical practice, Fig. 4g summarizes the results of moduli measured on the cheek areas and fingertip joint (near the nail plate) in human participants (details in Supplementary Fig. 30). As an example of the former, literature

reports indicate that the combined thickness of the epidermis and dermis is ~1.8 mm in the cheek region[53], and that other tissues (that is, superficial fat and muscle) appear beneath the dermis. Measurements using devices with *D* of 3 mm and of 1.5 mm yield V_S values of 28.7 μV and 19.3 μV, respectively, on the cheek. By utilizing the simulation curves of V_S for both cases from Fig. 4e and locating the intersection point as in Supplementary Fig. 30a, the cheek moduli are 248 kPa for the skin layer with a thickness of 1.8 mm and 59 kPa for inner tissues (blue in Fig. 4g). These measured moduli are consistent with values reported for the cheek region[31] and associated superficial fat in humans[30].

In addition to body areas such as the cheek, which has a comparatively large tissue thicknesses, measurements on regions where bones lie near the surface (for example, hand joints and the fingertip dorsum), where the tissue structure is thin, are of particular interest in clinical diagnosis and treatment of dermal pathologies such as scleroderma[5]. As an example, consider a simple estimate of the combined thickness of skin and tissues (~3 mm; ~2 mm for the skin and
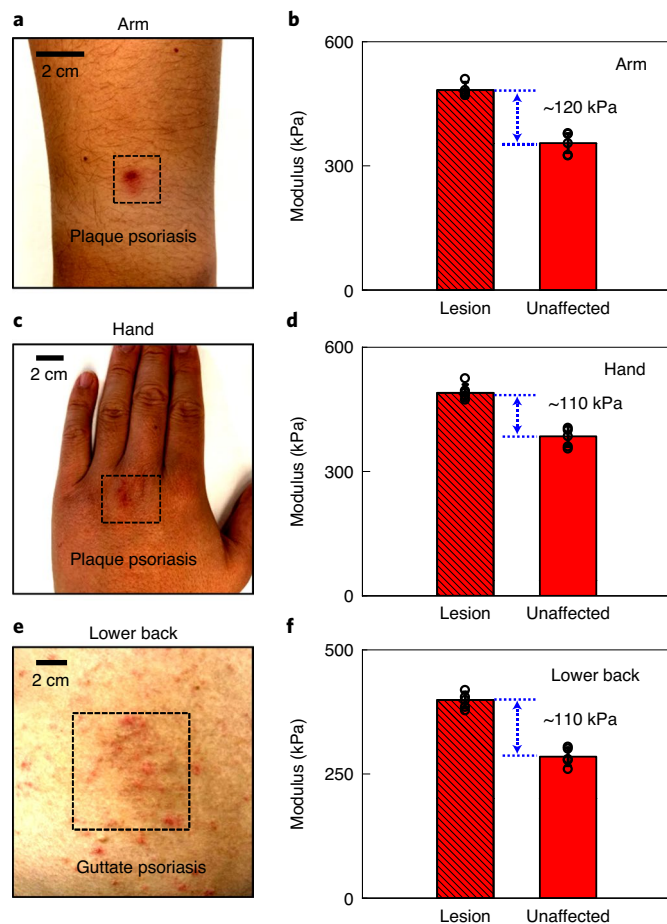
Fig. 5 | Measurements of skin lesions via miniaturized designs of the EMM sensors. a,c,e, Photographs of skin lesions associated with psoriasis on the arm (**a**), hand (**c**) and lower back (**e**). The dashed squares highlight the lesions, including symptoms of plaque psoriasis and guttate psoriasis. **b,d,f,** Measurements of skin lesions performed with a miniaturized EMM device design on the arm (**b**), hand (**d**) and back (**f**) of a representative patient. The modulus variations between unaffected skin and lesion regions are ~120 kPa, ~110 kPa and ~110 kPa, respectively. Error bars correspond to the standard deviation for five measurements within a representative participant, with corresponding centre values and dispersion measure shown.

~1 mm for the underlying tissues) in the fingertip joint near the nail plate of a volunteer[37] (Supplementary Fig. 31). Measurements with the EMM sensors yield V_S values of 27.1 µV ($D = 3$ mm) and 18.2 µV ($D = 1.5$ mm), corresponding to modulus values of 316 kPa for the skin layer and 67 kPa for inner tissues at this region of the body (red in Fig. 4g and Supplementary Fig. 30b). These results agree with those determined using conventional approaches[30,31]. Such findings demonstrate that a combined set of EMM sensors with appropriate D allows modulus characterization for multilayer biological targets with different thicknesses, across a wide range that involves not only bulk geometries (deep tissue scale) but also near-surface regions (superficial depth).

Compared with measurements that rely on large magnets for deep-tissue biomechanics (characteristic depth of ~8 mm), the miniaturized design yields information on skin mechanics with a focus on the near-surface structure (characteristic depth of ~1.6 mm). Measurements at such depths are relevant to many types of skin lesions (typically located within ~2-mm depth in skin), extending to

clinical evaluations presented in Supplementary Fig. 27. Specifically, variations in this near-surface modulus between lesion regions and unaffected skin are larger than those associated with measurements at greater depths, as shown in Fig. 5. Results from the arm, hand and back of patients with psoriasis (Fig. 5a,c,e) indicate near-surface modulus variations of ~110 kPa in each location (Fig. 5b,d,f), which are approximately two times larger than those measured at greater depths, using the initial device design (8-mm-diameter magnet design; Supplementary Fig. 27).

Interconnected arrays of devices for spatial mapping of the modulus. Multiple EMM sensors can be used separately, as described above, or they can be configured into arrays, as show in Fig. 6. Here, Fig. 6a presents a photograph of a collection of strain gauges printed onto a polymer substrate before interconnection (fabrication procedures described in the Methods), highlighting the mechanical flexibility (Supplementary Fig. 32) of the array for wrapping areas of interest across the body, as shown in Fig. 6b (the back of a male volunteer, aged 32 years). Figure 6c presents a schematic illustration of a 4×4 array of this type (4 columns, 4 rows, area of ~100 cm², thickness of ~2.5 mm) after assembly of vibratory actuators (Supplementary Fig. 33). Figure 6d summarizes an equivalent circuit diagram of the system. Interconnection to multiplexers allows rapid readout of signals from each unit cell in a time sequence controlled by a data acquisition (DAQ) system that features a minimal number of addressing wires, with capabilities for defining the frequencies and amplitudes of input voltages to each EMM sensor via a function generator as a power supply (Supplementary Fig. 34). Details are provided in the Supplementary Information.

The resulting multiplexed system can perform fast mapping of elastic moduli on curved, soft surfaces of tissues under quasi-static conditions. As an example, Fig. 6e shows results from measurements of elastic moduli across the back (Fig. 6b) during relaxed (left) and tensed states (right) associated with muscle contraction. Here, the actuator array (50 Hz, 5 V sine wave) produces signals from the underlying gauge array. Each unit cell corresponds to an elastic modulus value determined from an individual EMM sensor with a corresponding spatial resolution of ~1.5 cm². Stretching the trapezius muscle (red frame in Fig. 6e) of the back in the tensed condition (right of Fig. 6e) leads to spatial variations of increased moduli associated with activation of this targeted muscle group. Specifically, the average modulus for the tensed condition corresponds to ~430 kPa compared with ~310 kPa for the relaxed state, which is consistent with expectations and recent literature[54]. These results indicate the potential application of multiple devices in different directions and positions for measuring gradient feature of tissues with distributed lesion regions. Challenges, however, remain regarding high spatio-temporal resolution and scalability for precise measurements.

Outlook
We have established the materials, device designs and integration schemes for a biointegrated electromechanical system that can perform accurate, mechanical characterization of soft biological tissues in a noninvasive and rapid manner. Detailed experimental and simulated investigations highlight the various features of device operation with a wide range of soft biomaterials and multilayer samples and at various locations across the human body under different conditions. Careful design of the device and integration of arrays of sensors support evaluations of depth-dependent properties and spatial mapping, respectively. These findings potentially form the basis for routine monitoring of variations in elastic moduli for the diagnosis and treatment of various disease states and are applicable to nearly all parts of the human body. Particularly promising opportunities lie in dermatology, where the data produced by these devices can assist in diagnosis, treatment tracking and disease monitoring, as well as in aspects of aesthetic dermatology and of
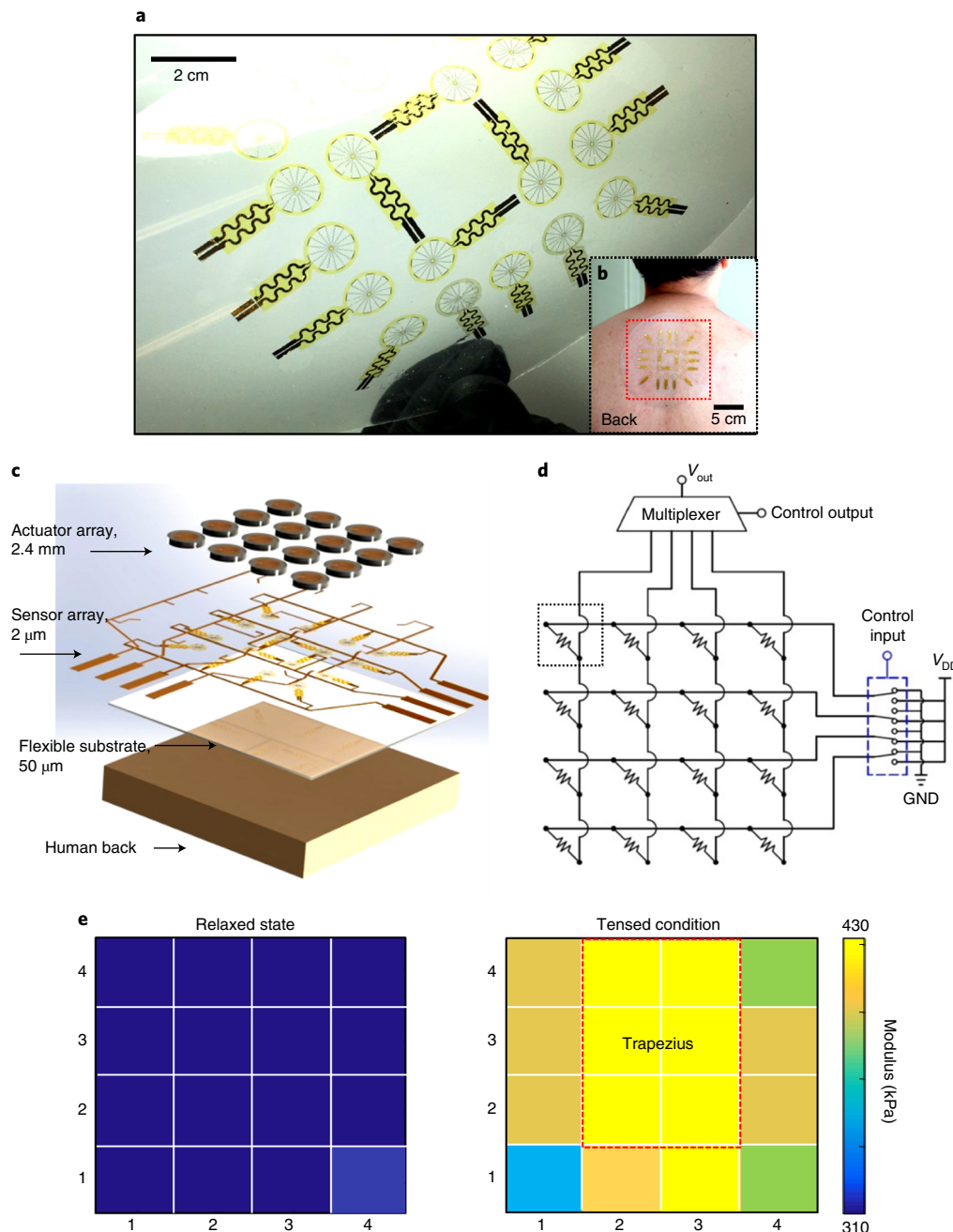
Fig. 6 | Multiplexed arrays of EMM sensors for spatial mapping of tissue modulus. a, Photograph of a collection of strain gauges printed on a thin film of PDMS. **b**, Photograph of the gauge array laminated onto the back of a participant. The red frame highlights the device area. **c**, Exploded-view schematic illustration of the layer configuration of a 4 × 4 array of sensors. **d**, Schematic illustration of the multiplexing circuit for the array mapping system. The dashed square corresponds to a unit cell. V_{DD}, supply voltage; GND, grounding voltage. **e**, Large-area spatial mapping of moduli obtained with this system while mounted on the back during a relaxed state (left) and tensed condition (right). Red frame corresponds to the estimated location of the trapezius muscle.

the recovery from surface wounds. Additional possibilities are in the evaluation of the mechanical properties of the skin in a variety of physical conditions, with an emphasis on age dependence[2] and on the relationship between biomechanics and functionality[41]. The results may serve as predictors of the potential for reactions of the skin to ageing, hydration loss and associated disorders, and could further establish the role of the skin in defining health status. Future work might also include efforts in advanced materials and designs for improved sensitivities, in engineering systems as wearables for

the continuous monitoring of patients during daily activities and in approaches for obtaining precise measurements of gradient features of tissues with high spatiotemporal resolution spanning the area of a single device by exploiting measurements across different arms of the filamentary serpentine design of the strain gauge.

Methods

Fabrication of sheets of strain gauges. As shown in Supplementary Fig. 1, the fabrication began with the formation of isolated strain gauges on a 4-inch silicon

wafer (100 mm in diameter, 500-μm thick; University Wafer) or a glass wafer (1-mm thick; VWR Vistavision). After cleaning the substrate surface via RCA processes, a thin, spin-cast film of PMMA (~500-nm thick; MicroChem) served as the sacrificial layer on the substrate and support for a spin-cast layer of polyimide (1-μm thick; PI-2545, HD MicroSystems). Electron-beam evaporation of Cr/Au (5/100 nm) and photolithographically patterning defined the electrical traces and sensing regions, with simple fabrication steps at high yield. The serpentine patterns of the traces also improved the fabrication yields. A second layer of polyimide (1-μm thick) encapsulated these features. Photolithography and reactive ion etching with O_2 isolated the devices into an open mesh structure (Supplementary Fig. 3). Subsequent processing released the gauge array from the handle wafer by immersion into acetone for 18 h to remove the sacrificial layer of PMMA. Transfer printing via a water-soluble tape (Grainger), followed by deposition of adhesive layers (Ti/SiO$_2$, electron-beam evaporation, 5/50-nm thick), allowed delivery of selected sets of devices from this array onto a foreign substrate coated with thin layers of PDMS (~30 μm; Sylgard 184, Dow Corning). Here, ultraviolet ozone (UVO) treatment of the surfaces of the devices and the top surfaces of the PDMS enabled strong bonding on contact. Peeling the material stack from the temporary substrate yielded a piece of flexible electronics as the basis for the strain gauges with excellent mechanical properties (Supplementary Fig. 5a). Detailed information on the fabrication processes and the transfer-printing technology is provided in Supplementary Fig. 2a, with a cross-sectional view of the strain gauge with a thickness of ~32 μm. Fabrication of multiple gauges and repetitive transfer printing onto a large-area layer of PDMS formed an array of such devices (Fig. 6a). Subsequent external wire connections relied on flexible cables and heat-seal connectors (Elform) to printed circuit boards for measurements, as shown Supplementary Fig. 4.

Assembly with vibratory actuators. Assembly of the vibratory actuators onto these gauges completed the integration to yield components with capabilities for measuring the elastic modulus. Procedures for assembly of the vibratory actuator exploited schemes described elsewhere[26]. Briefly, the first step involved immersing a Cu coil (wire diameter of 50 μm, 240 turns, with an inner diameter of the coil of 2 mm and an outer diameter of 12 mm; Yisu Electronics) into a layer of PDMS (diameter of 18 mm, 200-μm thick; 10:1 weight ratio of crosslinker) with the ends of the wire exposed to allow for external connection. The structure was then cured at 70 °C overnight. Next, the ring-shaped PDMS shell was cut into a suitable size (inner and outer diameter of 12 mm and 18 mm, respectively, 2.4-mm thick) and then bonded onto the coil–PDMS structure via a commercial adhesive (Kwik-Sil, World Precision Instruments). In parallel, a nickel-coated neodymium magnet (8 mm in diameter, 1.5-mm thick) was mounted on the centre of a polyimide disc (18 mm in diameter, 75-μm thick) with a strong dual-side adhesive (Kapton, DuPont). Carefully aligning the coil–PDMS ring and magnet–polyimide disc yielded a vibratory actuator, bonded together with a silicone adhesive applied on the contacting area (Kwik-Sil, World Precision Instruments). The final step involved deposition of a layer of SiO$_2$ (electron-beam evaporation, 100-nm thick) on the bottom surface of a polyimide disc across the ring-shaped area only (Fig. 1a). UVO treatment of the bottom surfaces of the actuator (polyimide-disc side) and the top surfaces of the fabricated gauge led to a strong bonding interface on contact to complete the assembly of the actuator and gauge. Detailed information for the assembly of the actuator and integration with the strain gauge is presented in Supplementary Fig. 2b, with a cross-sectional view with total thickness of ~2.5 mm. In this manner, the magnet of the actuator can vibrate in an out-of-plane direction in the ring-shaped PDMS shell, yielding pressure on the contacting tissue. The resulting overall system can directly laminate onto curved surfaces in intimate contact, with stable measurements, as shown in Supplementary Fig. 7.

Measurement set-up and operational principles. The measurement set-up included two areas of focus: the actuation and the sensor (schematic illustration shown in Supplementary Fig. 4). For quasi-static measurements, an output channel from a lock-in amplifier (SRS SR830, Stanford Research) was connected to the coil of the EMM sensor to deliver a sine-wave voltage (V_A, ± 5 V) with well-defined frequency and amplitude. The resultant current through the coil generated magnetic fields and associated time-dependent Lorentz forces to drive actuation and vibration of the magnet mounted on the thin polyimide disc. The result yielded a mechanism for imparting pressure onto the contacting tissues (Supplementary Fig. 12). The associated deformation of these tissues yielded strains distributed over the metal traces of the gauge. These responses allowed determination of the elastic modulus of the tissue. A constant current delivered from a current source (Keithley 6221, Tektronix) to the strain gauge (I_S) provided an input channel to the lock-in amplifier to capture the amplitudes of periodic variations in the resistance of the strain gauge as a sensing voltage (V_S) at the frequency of the vibration. Similarly, for dynamic measurements, a DAQ system (National Instrument) interfaced by wired connections to the sensor captured dynamic recordings of V_S at a sampling frequency of 5 Hz during actuation of the system.

Procedures for bending tests and soak tests. EMM sensors can establish gentle interfaces to soft, curved biological tissues, with capabilities of stable

electrical performance during immersion in biofluids. Bending tests are shown in Supplementary Fig. 7, where the systems intimately couple onto cylindrical substrates of artificial skin layers (PDMS, 200 kPa) with different curvatures, all with a characteristic depth of over 8 mm at the contacting location. The value of V_S remained unchanged at bending radii ranging from 4 cm to infinity (Supplementary Fig. 7) due to the neutral mechanical plane at the tissue interface.

Soak tests involved electrical measurements of devices during immersion in artificial sweat solution (pH 4.5, Pickering Laboratories) at elevated temperatures (50 °C). During the tests, the gauges, consisting of a trilayer structure of polyimide–metal traces–polyimide (1-μm–100-nm–1-μm thick), were mounted on a thin layer of PDMS with a weight ratio of crosslinker of 40:1. A thin, waterproof layer of Tagederm film (3M) encapsulated the front side the device, as shown in Supplementary Fig. 6c. Measurements demonstrated stable electrical performance during 7 days of immersion.

Preparation of artificial skin samples. Drop casting thick layers of PDMS with various thicknesses in a glass Petri dish formed artificial skin samples for purposes of validating the device operation (Supplementary Fig. 11a). These PDMS samples (area of 5 × 5 mm^2) involved different weight ratios of crosslinker to base, ranging from 3:1 to 60:1, all cured at room temperature over a day. As described in previous publications[20,21], the resulting artificial skins exhibit a range of elastic moduli. Viscoelastic effects can be neglected during measurements with actuation frequencies less than 100 Hz[20]. The effects of inertia are negligible because of the low frequencies, such that the measurements on these artificial skin samples and biomaterials can be considered quasi-static[21].

Measurement of elastic moduli using an in situ bioindenter and DMA. An in situ bioindenter (Hysitron Biosoft Indenter, Bruker) allowed quantitative analyses of the elastic moduli for each sample used for this work, including hydrogel, porcine skin (dermis side) and PDMS artificial skins. The measurement relied on a 20-μm-diameter spherical probe to indent the surface of a test sample, whereby the loading force as a function of the probe displacement was continuously recorded (normal bit force resolution, ~1 nN). The Hertz model was fitted to the elastic regime of the collected data to yield the final elastic modulus. As an example, measurement results for a set of PDMS artificial skin samples (dimension of 5 mm × 5 mm × 1 cm (length × width × thickness)) is shown in Supplementary Fig. 11b as a function of weight ratios of crosslinker. For instance, PDMS samples with a weight ratio of crosslinker to base as 15:1 correspond to a measured elastic modulus of ~500 kPa. Tests for porcine skin involved measurements with indentation on the dermis side. The DMA measurements (Q800, TA Instruments) used a film tension clamp in ambient conditions and a range of small strains (<10%). Samples for such measurements were cut into size of 1 cm × 5 mm × 1 mm (length × width × thickness).

Visualization of actuator operation. The vibratory amplitude represents a key parameter for device operation during mechanical measurements. A high-speed, high-resolution camera can capture a video in slow motion to allow for direct visualization of the actuators, including the amplitudes and orientations of the vibratory motions, as shown in the Supplementary Video 1. Similar procedures are used in other recently reported studies[25]. The results of vibratory amplitudes show relationships with frequencies of f and input voltages of V_A. In addition, the force generated by the actuator during actuation was measured via a flexible piezoresistive force sensor (FlexiForce); details are given in Supplementary Fig. 12.

Preparation of hydrogel samples and porcine skins with different hydration levels. Validation studies involved measurements of hydrogels and abdominal skin from porcine models, both with different hydration levels. For the hydrogel, a set of samples were synthesized by mixing different amounts (wt%) of poly(ethyleneglycol) diacrylate (Sigma-Aldrich) and de-ionized water. Powders of methylpropiophenone (2-hydroxy-4′-(2-hydroxyethoxy)-2-methylpropiophenone, ~0.6 wt%, Sigma-Aldrich) served as the initiator in the solution mixture, followed by UVO treatment for rapid curing in a Petri dish as the mould (area of 25 cm^2, 4-mm thick), with different elastic moduli for each hydration level. For the porcine skin, fresh samples from the abdominal region were cut (3 × 4 cm^2, 2-mm thick) and baked at 50 °C in an oven for over 48 h to evaporate the water content inside. The resulting weight of W_0 defined a hydration level of 0. Subsequently, submerging the samples into Dulbecco's phosphate-buffered saline (DPBS) solution at 37 °C for sufficiently long periods (~1 day) yielded fully saturated samples, corresponding to a maximum hydration state, with a weight of W and a hydration level that can be calculated as the percentage $(W − W_0)/W$. Similarly, different time scales for immersion in DPBS solution yielded samples with different hydration levels. A bioindenter was used to evaluate the elastic modulus of these samples.

Information for clinical tests and simulated evaluation. All participants for the study were fully voluntary and submitted the informed consent before tests. The research protocol was approved by Northwestern University's Institutional Review Board and the Northwestern Memorial Hospital (protocol number STU00206331-CR003) and registered on ClinicalTrials.gov (registration number

NCT03461549). Twenty volunteers (five young: 25–32 years old; five old: 60–68 years old) were recruited for studies of healthy skin without skin lesions. Among them, five have high BMI and five have low BMI. Five patients with skin disorders such as plaque psoriasis were involved in clinical tests, as shown in Supplementary Fig. 27. The pathological symptoms included red, thick patches of skin lesion (typically over 8 mm in diameter) with low hydration levels across the skin surface, and can be detected through physical palpations with detectable differences in skin properties such as stiffness and thickness. All of these volunteers and patients were at rest during the measurements.

After a process of cleaning pre-selected skin areas (lesion and healthy) by gentle rubbing with alcohol wipes, the EMM sensors were mounted onto the relevant skin areas followed by conformal coverage with a medical dressing (Tegaderm, 3M) to secure device placement. The placement of the sensors was performed by research staff and/or medical doctors. The EMM sensors were pre-connected to a DAQ system (including a locking-in amplifier and a current source) located within the operational room. Data recording began after 10 s of system warm-up to ensure stable operation. Each participant performed 1 min of measurement in a resting position. Data were collected and stored for further data analysis on a tablet computer. Similar to the operation on participants, a corresponding measurement that simulated clinical tests on an artificial-skin model is shown in Supplementary Fig. 26.

Reporting Summary. Further information on research design is available in the Nature Research Reporting Summary linked to this article.

Data availability
The data supporting the results in this study are available within the paper and its Supplementary Information. The raw patient data are available from the authors, subject to approval from Northwestern University's Institutional Review Board.

References
1. Joodaki, H. & Panzer, M. B. Skin mechanical properties and modeling: a review. *Proc. Inst. Mech. Eng. H* **232**, 323–343 (2018).
2. Pawlaczyk, M., Lelonkiewicz, M. & Wieczorowski, M. Age-dependent biomechanical properties of the skin. *Postepy Dermatol. Alergol.* **5**, 302–306 (2013).
3. Pandya, H. J., Chen, W., Goodell, L. A., Foran, D. J. & Desai, J. P. Mechanical phenotyping of breast cancer using MEMS: a method to demarcate benign and cancerous breast tissues. *Lab Chip* **14**, 4523–4532 (2014).
4. Leblanc, N. et al. Durometer measurements of skin induration in venous disease. *Dermatol. Surg.* **23**, 285–287 (1997).
5. Khanna, D. et al. Standardization of the modified Rodnan skin score for use in clinical trials of systemic sclerosis. *J. Scleroderma Relat. Disord.* **2**, 11–18 (2017).
6. Batisse, D., Bazin, R. & Baldeweck, T. Influence of age on the wrinkling capacities of skin. *Skin Res. Technol.* **8**, 148–154 (2002).
7. Diridollou, S. et al. Sex and site dependent variations in thickness and mechanical properties of human skin in vivo. *Int. J. Cosmet. Sci.* **22**, 421–435 (2000).
8. Kashibuchi, N., Hirai, Y., O'Goshi, K. & Tagami, H. Three-dimensional analyses of individual corneocytes with atomic force microscope: morphological changes related to age, location and to the pathologic skin conditions. *Skin Res. Technol.* **8**, 203–211 (2002).
9. Lulevich, V., Zink, T., Chen, H.-Y., Liu, F.-T. & Liu, G. Cell mechanics using atomic force microscopy-based single-cell compression. *Langmuir* **22**, 8151–8155 (2006).
10. Zheng, Y. & Mak, A. F. T. Effective elastic properties for lower limb soft tissues from manual indentation experiment. *IEEE Trans. Rehabil. Eng.* **7**, 257–267 (1999).
11. Diridollou, S. et al. In vivo model of the mechanical properties of the human skin under suction. *Skin Res. Technol.* **6**, 214–221 (2000).
12. Hendriks, F. M. et al. A numerical-experimental method to characterize the non-linear mechanical behaviour of human skin. *Skin Res. Technol.* **9**, 274–283 (2003).
13. Agache, P. G., Monneur, C., Leveque, J. L. & Rigal, J. D. Mechanical properties and Young's modulus of human skin in vivo. *Arch. Dermatol. Res.* **269**, 221–232 (1980).
14. Fischer-Cripps, A. C. Critical review of analysis and interpretation of nanoindentation test data. *Surf. Coat. Technol.* **200**, 4153–4165 (2006).
15. Gennisson, J. L. et al. Assessment of elastic parameters of human skin using dynamic elastography. *IEEE Trans. Ultrason. Ferroelectr. Freq. Control* **51**, 980–989 (2004).
16. Castera, L., Vilgrain, V. & Angulo, P. Noninvasive evaluation of NAFLD. *Nat. Rev. Gastroenterol. Hepatol.* **10**, 666–675 (2013).
17. Manduca, A. et al. Magnetic resonance elastography: non-invasive mapping of tissue elasticity. *Med. Image Anal.* **5**, 237–254 (2001).
18. Rogers, J. A., Someya, T. & Huang, Y. Materials and mechanics for stretchable electronics. *Science* **327**, 1603–1607 (2010).
19. Huang, C.-T., Shen, C.-L., Tang, C.-F. & Chang, S.-H. A wearable yarn-based piezo-resistive sensor. *Sens. Actuators A* **141**, 396–403 (2008).
20. Dagdeviren, C. et al. Conformal piezoelectric systems for clinical and experimental characterization of soft tissue biomechanics. *Nat. Mater.* **14**, 728–736 (2015).
21. Yu, X. et al. Needle-shaped ultrathin piezoelectric microsystem for guided tissue targeting via mechanical sensing. *Nat. Biomed. Eng.* **2**, 165–172 (2018).
22. Lipomi, D. J. et al. Skin-like pressure and strain sensors based on transparent elastic films of carbon nanotubes. *Nat. Nanotechnol.* **6**, 788–792 (2011).
23. Son, D. et al. Multifunctional wearable devices for diagnosis and therapy of movement disorders. *Nat. Nanotechnol.* **9**, 397–404 (2014).
24. Yeh, W.-C. et al. Elastic modulus measurements of human liver and correlation with pathology. *Ultrasound Med. Biol.* **28**, 467–474 (2002).
25. Yu, X. et al. Skin-integrated wireless haptic interfaces for virtual and augmented reality. *Nature* **575**, 473–479 (2019).
26. He, W. et al. Study on Young's modulus of thin films on Kapton by microtensile testing combined with dual DIC system. *Surf. Coat. Technol.* **308**, 273–279 (2016).
27. Kroner, E., Maboudian, R. & Arzt, E. Adhesion characteristics of PDMS surfaces during repeated pull-off force measurements. *Adv. Eng. Mater.* **12**, 398–404 (2010).
28. Zhang, Y. et al. Experimental and theoretical studies of serpentine microstructures bonded to prestrained elastomers for stretchable electronics. *Adv. Funct. Mater.* **24**, 2028–2037 (2014).
29. Swanson, E. C., Weathersby, E. J., Cagle, J. C. & Sanders, J. E. Evaluation of force sensing resistors for the measurement of interface pressures in lower limb prosthetics. *J. Biomech. Eng.* **141**, 101009 (2019).
30. Li, C., Guan, G., Reif, R., Huang, Z. & Wang, R. K. Determining elastic properties of skin by measuring surface waves from an impulse mechanical stimulus using phase-sensitive optical coherence tomography. *J. R. Soc. Interface* **9**, 831–841 (2012).
31. Kalra, A., Lowe, A. & Al-Jumaily, A. M. Mechanical behaviour of skin: a review. *J. Mater. Sci. Eng.* **5**, 1000254 (2016).
32. Geerlings, M. et al. In vitro indentation to determine the mechanical properties of epidermis. *J. Biomech.* **44**, 1176–1181 (2011).
33. Wang, L. et al. Ultrasoft and highly stretchable hydrogel optical fibers for in vivo optogenetic modulations. *Adv. Optical Mater.* **6**, 1800427 (2018).
34. Sun, J. Y. et al. Highly stretchable and tough hydrogels. *Nature* **489**, 133–136 (2012).
35. Garcia, M. & Angelini, T. E. A method for eliminating the need to know when contact is made with soft surfaces: data processing and error analysis. *Biotribology* **20**, 100109 (2019).
36. Leong, S. S. et al. Stiffness and anisotropy effect on shear wave elastography: a phantom and in vivo renal study. *Ultrasound Med. Biol.* **46**, 34–45 (2019).
37. Pejovi-Mili, A., Brito, J. A., Gyorffy, J. & Chettle, D. R. Ultrasound measurements of overlying soft tissue thickness at four skeletal sites suitable for in vivo X-ray fluorescence. *Med. Phys.* **29**, 2687–2691 (2002).
38. Akkus, O., Oguz, A., Uzunlulu, M. & Kizilgul, M. Evaluation of skin and subcutaneous adipose tissue thickness for optimal insulin injection. *J. Diabetes Metab.* **3**, 1000216 (2012).
39. Kiliaridis, S. & Kälebo, P. Masseter muscle thickness measured by ultrasonography and its relation to facial morphology. *J. Dent. Res.* **70**, 1262–1265 (1991).
40. Jain, S. M., Pandey, K., Lahoti, A. & Rao, P. K. Evaluation of skin and subcutaneous tissue thickness at insulin injection sites in Indian, insulin naive, type-2 diabetic adult population. *Indian J. Endocrinol. Metab.* **17**, 864–870 (2013).
41. Pedersen, L. & Jemec, G. B. E. Mechanical properties and barrier function of the skin. *Acta Derm. Venereol.* **86**, 308–311 (2006).
42. Laiacona, D. et al. Non-invasive in vivo quantification of human skin tension lines. *Acta Biomaterialia* **88**, 141–148 (2019).
43. Jacquet, E., Josse, G., Khatyr, F. & Garcin, C. A new experimental method for measuring skin's natural tension. *Skin Res. Technol.* **14**, 1–7 (2008).
44. Storchle, P. et al. Standardized ultrasound measurement of subcutaneous fat patterning: high reliability and accuracy in groups ranging from lean to obese. *Ultrasound Med. Biol.* **43**, 427–438 (2017).
45. Yoshitake, Y., Takai, Y., Kanehisa, H. & Shinohara, M. Muscle shear modulus measured with ultrasound shear-wave elastography across a wide range of contraction intensity. *Muscle Nerve* **50**, 103–113 (2014).
46. Shinohara, M., Sabra, K., Gennisson, J., Fink, M. & Tanter, M. Real-time visualization of muscle stiffness distribution with ultrasound shear wave imaging during muscle contraction. *Muscle Nerve* **42**, 438–441 (2010).
47. Lewis-Beck, C., Abouzaid, S., Xie, L., Baser, O. & Kim, E. Analysis of the relationship between psoriasis symptom severity and quality of life, work productivity, and activity impairment among patients with

moderate-to-severe psoriasis using structural equation modeling. *Patient Prefer. Adherence* **7**, 199–205 (2013).

48. Kim, S. D., Huh, C. H., Seo, K. I., Suh, D. H. & Youn, J. I. Evaluation of skin surface hydration in Korean psoriasis patients: a possible factor influencing psoriasis. *Clin. Exp. Dermatol.* **27**, 147–152 (2002).

49. Dobrev, H. In vivo study of skin mechanical properties in psoriasis vulgaris. *Acta Derm. Venereol.* **80**, 263–266 (2000).

50. Chen, C. et al. Ultrasound assessment of skin thickness and stiffness: the correlation with histology and clinical score in systemic sclerosis. *Arthritis Res. Ther.* **43**, 427–438 (2017).

51. Wang, L., Yan, F., Yang, Y., Xiang, X. & Qiu, L. Quantitative assessment of skin stiffness in localized scleroderma using ultrasound shear-wave elastography. *Ultrasound Med. Biol.* **43**, 1339–1347 (2017).

52. Samani, A., Zubovits, J. & Plewes, D. Elastic moduli of normal and pathological human breast tissues: an inversion-technique-based investigation of 169 samples. *Phys. Med. Biol.* **52**, 1565–1576 (2007).

53. Kim, T.-S. et al. Regional thickness of facial skin and superficial fat: application to the minimally invasive procedures. *Clin. Anat.* **32**, 1008–1018 (2019).

54. Annaidh, A. N., Bruyère, K., Destrade, M., Gilchrist, M. D. & Otténio, M. Characterization of the anisotropic mechanical properties of excised human skin. *J. Mech. Behav. Biomed.* **5**, 139–148 (2012).

Author contributions

E.S., Z.X., W.B., X.Y., Y.H. and J.A.R. designed the research. E.S., Z.X., W.B., H.L., X.N., Y.X., J.M.B., Y.L., H.-Y.C., J.-H.K., S.M., S.M.W., X.Z., D.J.M., M.H., S.X., J.-K.C., X.Y., Y.H. and J.A.R. performed the research. E.S., Z.X., W.B., B.J., R.A., K.Y., D.L., J.Z. Y.M., X.G., J.-K.C., X.Y., Y.H. and J.A.R. analysed the data. Z.X., E.S., B.J., R.A., X.G., Y.H. and J.A.R. performed structural designs and mechanical modelling. E.S., Z.X., W.B., X.Y., Y.H. and J.A.R. wrote the paper.

Competing interests

The authors declare no competing interests.

Additional information

Supplementary information The online version contains supplementary material available at https://doi.org/10.1038/s41551-021-00723-y.

Correspondence and requests for materials should be addressed to J.-K.C., X.Y., Y.H. or J.A.R.

Peer review information *Nature Biomedical Engineering* thanks Jianyong Ouyang, Levent Beker and the other, anonymous, reviewer(s) for their contribution to the peer review of this work.

Reprints and permissions information is available at www.nature.com/reprints.

nature research

Corresponding author(s): Jan-Kai Chang, Xinge Yu, Yonggang Huang and John A. Rogers

Last updated by author(s): Apr 6, 2021

Reporting Summary

Nature Research wishes to improve the reproducibility of the work that we publish. This form provides structure for consistency and transparency in reporting. For further information on Nature Research policies, see our Editorial Policies and the Editorial Policy Checklist.

Statistics

For all statistical analyses, confirm that the following items are present in the figure legend, table legend, main text, or Methods section.

n/a	Confirmed	
☐	☒	The exact sample size (n) for each experimental group/condition, given as a discrete number and unit of measurement
☐	☒	A statement on whether measurements were taken from distinct samples or whether the same sample was measured repeatedly
☐	☒	The statistical test(s) used AND whether they are one- or two-sided *Only common tests should be described solely by name; describe more complex techniques in the Methods section.*
☒	☐	A description of all covariates tested
☐	☒	A description of any assumptions or corrections, such as tests of normality and adjustment for multiple comparisons
☐	☒	A full description of the statistical parameters including central tendency (e.g. means) or other basic estimates (e.g. regression coefficient) AND variation (e.g. standard deviation) or associated estimates of uncertainty (e.g. confidence intervals)
☒	☐	For null hypothesis testing, the test statistic (e.g. F, t, r) with confidence intervals, effect sizes, degrees of freedom and P value noted *Give P values as exact values whenever suitable.*
☒	☐	For Bayesian analysis, information on the choice of priors and Markov chain Monte Carlo settings
☒	☐	For hierarchical and complex designs, identification of the appropriate level for tests and full reporting of outcomes
☐	☒	Estimates of effect sizes (e.g. Cohen's d, Pearson's r), indicating how they were calculated

Our web collection on statistics for biologists contains articles on many of the points above.

Software and code

Policy information about availability of computer code

Data collection	The following software applications were used to collect data and to program the devices: lock-in amplifier (SRS SR830, Stanford Research), current source (Keithley 6221, Tektronix), and data acquisition (DAQ) system.
Data analysis	Data analysis and plotting were done with Origin and Adobe Premiere Pro.

For manuscripts utilizing custom algorithms or software that are central to the research but not yet described in published literature, software must be made available to editors and reviewers. We strongly encourage code deposition in a community repository (e.g. GitHub). See the Nature Research guidelines for submitting code & software for further information.

Data

Policy information about availability of data

All manuscripts must include a data availability statement. This statement should provide the following information, where applicable:

- Accession codes, unique identifiers, or web links for publicly available datasets
- A list of figures that have associated raw data
- A description of any restrictions on data availability

The data supporting the results in this study are available within the paper and its Supplementary Information. The raw patient data are available from the authors, subject to approval from Northwestern University's Institutional Review Board.

Field-specific reporting

Please select the one below that is the best fit for your research. If you are not sure, read the appropriate sections before making your selection.

☒ Life sciences ☐ Behavioural & social sciences ☐ Ecological, evolutionary & environmental sciences

For a reference copy of the document with all sections, see nature.com/documents/nr-reporting-summary-flat.pdf

Life sciences study design

All studies must disclose on these points even when the disclosure is negative.

Sample size	Sample sizes were chosen according to relevant reports in the literature.
Data exclusions	No data were excluded.
Replication	Experiments were replicated multiple times.
Randomization	Randomization was not required.
Blinding	The investigators completing the data analyses were blinded to the experimental groups.

Reporting for specific materials, systems and methods

We require information from authors about some types of materials, experimental systems and methods used in many studies. Here, indicate whether each material, system or method listed is relevant to your study. If you are not sure if a list item applies to your research, read the appropriate section before selecting a response.

Materials & experimental systems

n/a	Involved in the study
☒	☐ Antibodies
☒	☐ Eukaryotic cell lines
☒	☐ Palaeontology and archaeology
☐	☒ Animals and other organisms
☐	☒ Human research participants
☐	☒ Clinical data
☒	☐ Dual use research of concern

Methods

n/a	Involved in the study
☒	☐ ChIP-seq
☒	☐ Flow cytometry
☒	☐ MRI-based neuroimaging

Animals and other organisms

Policy information about studies involving animals; ARRIVE guidelines recommended for reporting animal research

Laboratory animals	Abdominal porcine skin.
Wild animals	The study did not involve wild animals.
Field-collected samples	The study did not involve samples collected from the field.
Ethics oversight	The experiments were conducted in accordance with the ethical guidelines of the National Institutes of Health, and was approved by Northwestern University's Institutional Review Board.

Note that full information on the approval of the study protocol must also be provided in the manuscript.

Human research participants

Policy information about studies involving human research participants

Population characteristics	Twenty volunteers (among them, five were 25–32 years old, and five 60–68 years old) were recruited for studies on normal healthy skin without any skin lesions. Five patients (age 25–35) with skin disorders such as plaque psoriasis were involved in studies with measurements on lesioned skin. Gender or other information for these participants were randomized.
Recruitment	Participation was fully voluntary, and all subjects provided informed consent before the tests.

| Ethics oversight | The research protocol was approved by Northwestern University's Institutional Review Board and the Northwestern Memorial Hospital, USA (Protocol Number: STU00206331-CR003). |

Note that full information on the approval of the study protocol must also be provided in the manuscript.

Clinical data

Policy information about clinical studies

All manuscripts should comply with the ICMJE guidelines for publication of clinical research and a completed CONSORT checklist must be included with all submissions.

| Clinical trial registration | The research protocol was registered on ClinicalTrials.gov (Registration Number: NCT03461549). |

| Study protocol | The full trial protocol can be accessed at https://clinicaltrials.gov/ct2/show/NCT03461549. |

| Data collection | The sensors were mounted onto the relevant skin areas. The placement of the sensors was carried out by research staff and/or medical doctors. The EMM sensors were pre-connected to a DAQ system (including a locking-in amplifier and a current source) located within the operational room. Data recording began after 10 s of system warm-up, to ensure stable operation. Each subject performed 1-min measurement in a resting position. Data were collected and stored for further data analysis on a tablet computer. |

| Outcomes | Primary outcome measure: measurement results based on modulus sensor.
Secondary outcome measures: Visual analogue scale of skin irritation. |